

PAPER • OPEN ACCESS

Impact of toroidal rotation on the resistive ballooning modes in ASDEX Upgrade tokamak

To cite this article: B Vanovac *et al* 2023 *Plasma Phys. Control. Fusion* **65** 095011

View the [article online](#) for updates and enhancements.

You may also like

- [CASTOR3D: linear stability studies for 2D and 3D tokamak equilibria](#)
E. Strumberger and S. Günter
- [Linear stability studies for a quasi-axisymmetric stellarator configuration including effects of parallel viscosity, plasma flow, and resistive walls](#)
E. Strumberger and S. Günter
- [Cascaded systems analysis of anatomic noise in digital mammography and dual-energy digital mammography](#)
Jesse Tanguay, Robert Lalonde, Thorarin A Bjarnason et al.

Impact of toroidal rotation on the resistive ballooning modes in ASDEX Upgrade tokamak

B Vanovac^{1,2,*} , J Puchmayr² , R Bielajew¹ , M Willensdorfer² ,
E Wolfrum² , M Cavedon^{2,3} , E Strumberger² , M G Dunne² , W Suttrop² 
and the ASDEX Upgrade Team^a

¹ Plasma Science and Fusion Center, Massachusetts Institute of Technology, Cambridge, MA 02139, United States of America

² Max-Planck-Institut für Plasmaphysik, 85748 Garching, Germany

³ Department of Physics 'G. Occhialini', University of Milan-Bicocca, Milan, Italy

E-mail: vanovac@mit.edu

Received 18 January 2023, revised 13 July 2023

Accepted for publication 20 July 2023

Published 1 August 2023



CrossMark

Abstract

In this work, we investigate the behavior of instabilities appearing between type-I edge localized modes (ELMs), with increasing neutral beam injection (NBI) power concomitant increase in toroidal rotation, and compare it to the modeling result of the linear magneto-hydrodynamic (MHD) code CASTOR3D. An injection of one NBI beam, increasing toroidal rotation, results in the mode slowing down from 12 kHz to 7 kHz, and its associated radial displacement decreases from 5 mm to 3.5 mm. In addition, modes shift radially outwards towards higher q , decreasing their poloidal mode numbers. The mode velocity is measured to be close to the $E \times B$ velocity with significant uncertainties. Through a set of CASTOR3D simulations with varying profiles, resistivity has been identified as the primary contributor to the growth rates. Only a small stabilizing effect due to toroidal rotation has been observed. While experimental results show a decrease of mode frequency with rotation, the opposite trend is observed in modeling. Reasons for discrepancies between modeling and experiment are discussed. Nevertheless, a main contributor to the mode frequency has been identified to be rotation velocity. CASTOR3D classifies modes as resistive ballooning modes as they do not appear unstable in ideal MHD.

Keywords: mode rotation, inter-ELM modes, resistive ballooning modes, pedestal, phase velocity, ECE Imaging, CASTOR3D

(Some figures may appear in colour only in the online journal)

1. Introduction

Various magneto-hydrodynamic (MHD) macro-instabilities at the plasma edge limit the achievable pedestal plasma pressure

^a See Stroth *et al* 2022 (<https://doi.org/10.1088/1741-4326/ac207f>) for the ASDEX Upgrade Team.

* Author to whom any correspondence should be addressed.



Original Content from this work may be used under the terms of the [Creative Commons Attribution 4.0 licence](https://creativecommons.org/licenses/by/4.0/). Any further distribution of this work must maintain attribution to the author(s) and the title of the work, journal citation and DOI.

and, consequently, limit the core performance. Another potential performance-limiting factor could be heat and particle transport caused by the micro-instabilities such as ion-temperature gradient [1], electron-temperature gradient (ETG) [2], trapped electron modes [3] and micro-tearing modes [4]. However, transport is not always performance-limiting. It can help keep the pedestal pressure below the critical value for the onset of the sudden pedestal collapse, type-I edge localized modes (ELMs) [5]. The type-I ELMs are accompanied by enormous heat loads onto the divertor and are identified as a threat to the machine's integrity when extrapolated to a larger machine [5]. Macro-instabilities in the form of

MHD modes and precursors also accompany Type-I ELMs, usually appearing milliseconds before the crash's onset. They might cause transport and influence the pedestal structure. Inter-ELM modes and ELM precursors to type-I ELMs have been observed on different machines and share some similarities with the precursor modes to type-III ELMs [6]. Examples are: palm tree mode [7], washboard modes at JET [8], ELM precursors at ASDEX Upgrade [9] and COMPASS-D [10]. In ASDEX Upgrade, simultaneous observations of high-frequency and low-frequency inter-ELM modes, appearing before type-I ELM crash, have been first reported in [11]. The detailed characterization of low (<20 kHz), high (200–300 kHz) and mid-frequency (50–100 kHz) inter-ELM modes is presented in [12–14]. From measurements of the toroidal and poloidal mode numbers, modes are inferred to be resonant at q -surfaces near the pedestal top, minimum radial electric field, and the separatrix, respectively. Magnetic pick-up coils measure all three frequency branches. However, the role of inter-ELM modes and precursors in regulating the pedestal stability and transport is still an open question.

One aspect impacting the MHD modes, particularly their stability, is altering the plasma rotation and shear. The effects have been identified in numerical experiments with different outcomes. The stabilizing effect of rotation on tearing modes is reported in [15]. The effect of the rotation on ideal and resistive modes can be both stabilizing and destabilizing, depending on the plasma and rotation profiles. It also has a substantial effect on the observed mode structure [16]. However, two-fluid MHD calculations with NIMROD show that increasing the edge plasma density enhances stabilization [17]. The work in [18], shows that resistive walls can stabilize modes with low toroidal mode number and plasma rotation. This wall stabilization leads to an experimentally significant increase in the beta limit. In [19], rotation is found to be stabilizing, but the overall effect depends on the rotation and pressure profile. In addition, active control of the pedestal with toroidal rotation is achieved in quiescent H-modes (QH-modes) [20], and rotation-induced sheared flow was shown to be stabilizing to very high- n MHD modes [21] where the most unstable mode moves to a longer wavelength.

In this paper, the NBI-injected beam power was varied to study the impact of the NBI-induced rotation on modes appearing in the plasma edge and between type-I ELMs. In the experiment, the change in the NBI beam power leads to changes in other plasma parameters, such as pressure gradient and temperature, which can further influence the mode behavior. Therefore, we compare these experimental results to the results of a linear MHD code CASTOR3D, where input parameters can be changed independently. We evaluate the changes in the typical mode characteristics and compare them to the numerical analysis result.

2. Diagnostics

Below, we describe an essential diagnostic suite at ASDEX Upgrade used for mode characterization: correlation electron

cyclotron emission (CECE) is used for the localization of the fluctuation; electron cyclotron emission (ECE) Imaging for the poloidal velocity measurements and mode structure; charge exchange recombination spectroscopy (CXRS) for measurements of toroidal flow and perpendicular $E \times B$ velocity. Electron density, temperature, and pressure profiles are obtained using an integrated data analysis (IDA) approach.

The CECE diagnostic at ASDEX Upgrade is a 24-channel heterodyne radiometer allowing temperature fluctuation measurements [22]. The basic principle relies on correlation analysis between two neighboring channels, and their spatial separation ensures decorrelated noise, therefore, measuring low amplitude turbulence ($\sim 1\%$). The lines of sight of the CECE system at ASDEX Upgrade are shared with the standard ECE system and cover a low field side midplane. Limitations of the ECE measurements and radiation transport effects across the plasma edge [23, 24] are considered when analyzing the ECE from the pedestal region.

The ECE Imaging (ECEI) system uses the same physical principles as ECE but has multiple poloidally distributed heterodyne radiometers. The plasma's electron cyclotron radiation is guided via a set of lenses and quasi-optically imaged onto a detector array. Each detector resolves eight radial channels so that the diagnostic delivers a two-dimensional image of temperature fluctuations [25, 26].

Plasma rotation is measured using the CXRS method [27]. Line radiation from the interaction between the neutral beam and injected impurities is used. Toroidal rotation is deduced from the spectral lines produced by charge transfer from neutral atoms into highly excited states of impurity ions. The ion temperature and flow velocity are obtained from the Doppler width and shift, respectively. In addition, the impurity density can be obtained from the radiance of the emission line. In ASDEX Upgrade, poloidal and toroidal CXRS systems provide poloidal and toroidal impurity rotation velocities, respectively [28].

Density, temperature, and pressure profiles are obtained using the framework of IDA [29, 30]. It provides a complete probabilistic model, including physical and statistical models of an integrated set of different diagnostics. It combines lithium beam emission spectroscopy, ECE, Thomson scattering, and deuterium cyanide laser interferometry in the standard diagnostic coordinate system.

3. The experiment

In ASDEX Upgrade, modes between type-I ELMs appear in the discharges with a heating power level just above the LH power threshold. In these scenarios, the ELM frequency is below 100 Hz, and this low repetition rate of ELMs allows for long periods between ELMs where modes can develop. Figure 1 shows the temporal evolution of one ECE channel measuring at $\rho_{\text{pol}} \approx 0.98$ and its spectrogram where modes at a frequency below 20 kHz are visible. An increase in the ECE

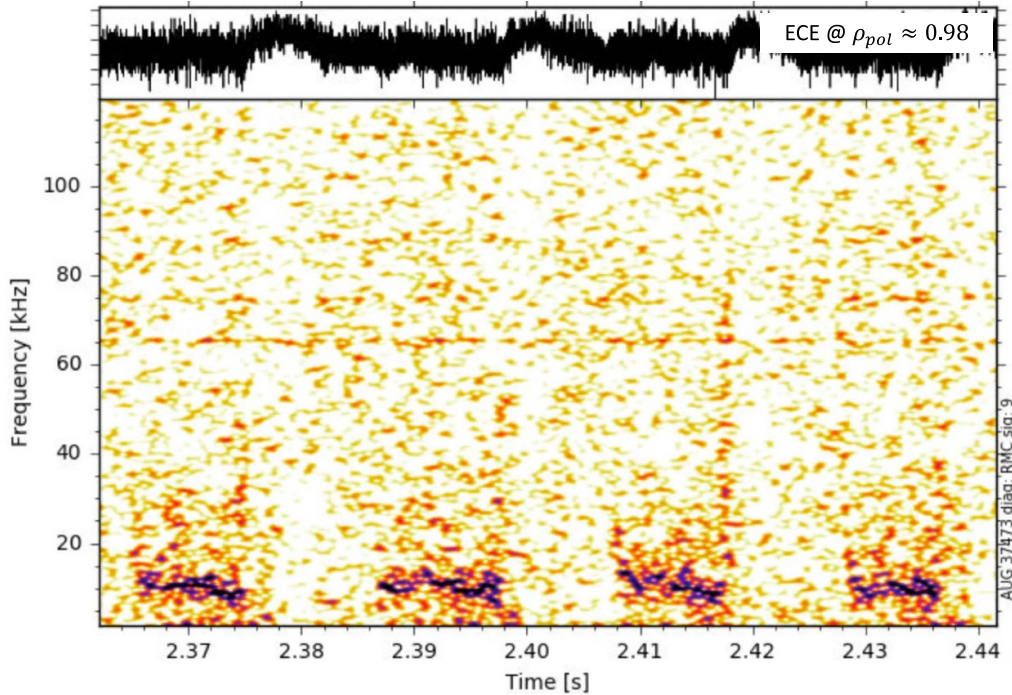


Figure 1. Temporal evolution of one ECE channel measuring at $\rho_{pol} \approx 0.98$ and its spectrogram showing modes at frequency below 20 kHz. An increase in the ECE signal corresponds to an ELM crash.

signal corresponds to an ELM crash. Modes show dynamic behavior, and their frequency can vary throughout their lifetime. Some of those general characteristics are elaborated in [31]. The most notable feature, reported in [31], is the correlation between the mode frequency and the heating power where the frequency of modes decreases with increasing heating power. This correlation is demonstrated in figure 2, where we show 15-time intervals featuring the mode's appearance. The highest frequency of modes is observed in the discharges where only electron cyclotron resonance heating (ECRH) and combined ECRH and ion cyclotron resonance heating (ICRH) heating are applied. The remaining points correspond to the variation in NBI heating. The ECRH heating was varied by about 0.5 MW for those remaining points. Therefore the majority of the power comes from the NBI beams. In this dataset, however, temperature, density, and pressure profiles differ significantly between the data points, and it is not possible to isolate the effect of the NBI and induced rotation alone. Therefore, this manuscript focuses on a single discharge with two different NBI heating phases manifesting in different rotation profiles. Although the rest of the plasma parameters are intended to stay constant, injecting additional beam power can cause slight changes in the pressure and temperature profile. Such small changes are difficult to separate within the experimental uncertainties, and the only possibility to separate those effects is numerically, as will be shown later in this manuscript. In the following, the mode frequency for the two cases are displayed in red and blue, corresponding to phases one and two, respectively.

To study the relationship between the NBI heating-induced toroidal rotation and mode behavior, we study a plasma

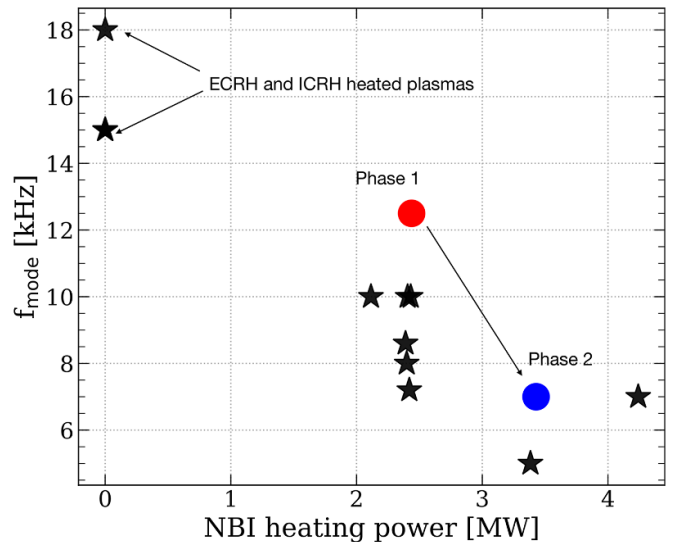


Figure 2. Mode frequency as a function of the NBI heating power. As marked in the upper left corner, the highest mode frequencies are obtained for ECRH and a combination of the ICRH and ECRH heating methods (zero NBI power). The red and the blue circle are the data points discussed in this manuscript.

scenario shown in figure 3. Heating power levels P (MW) from ECRH (blue) and NBI (red) systems are displayed in figure 3(a). The total heating power is shown as a black line. The outer plasma radius R_{aus} (black) and the upper triangularity δ_u (blue) are shown in figure 3(b). Edge (red) and core (blue) electron densities are constant throughout the discharge as shown in figure 3(c). ELM frequency is displayed in

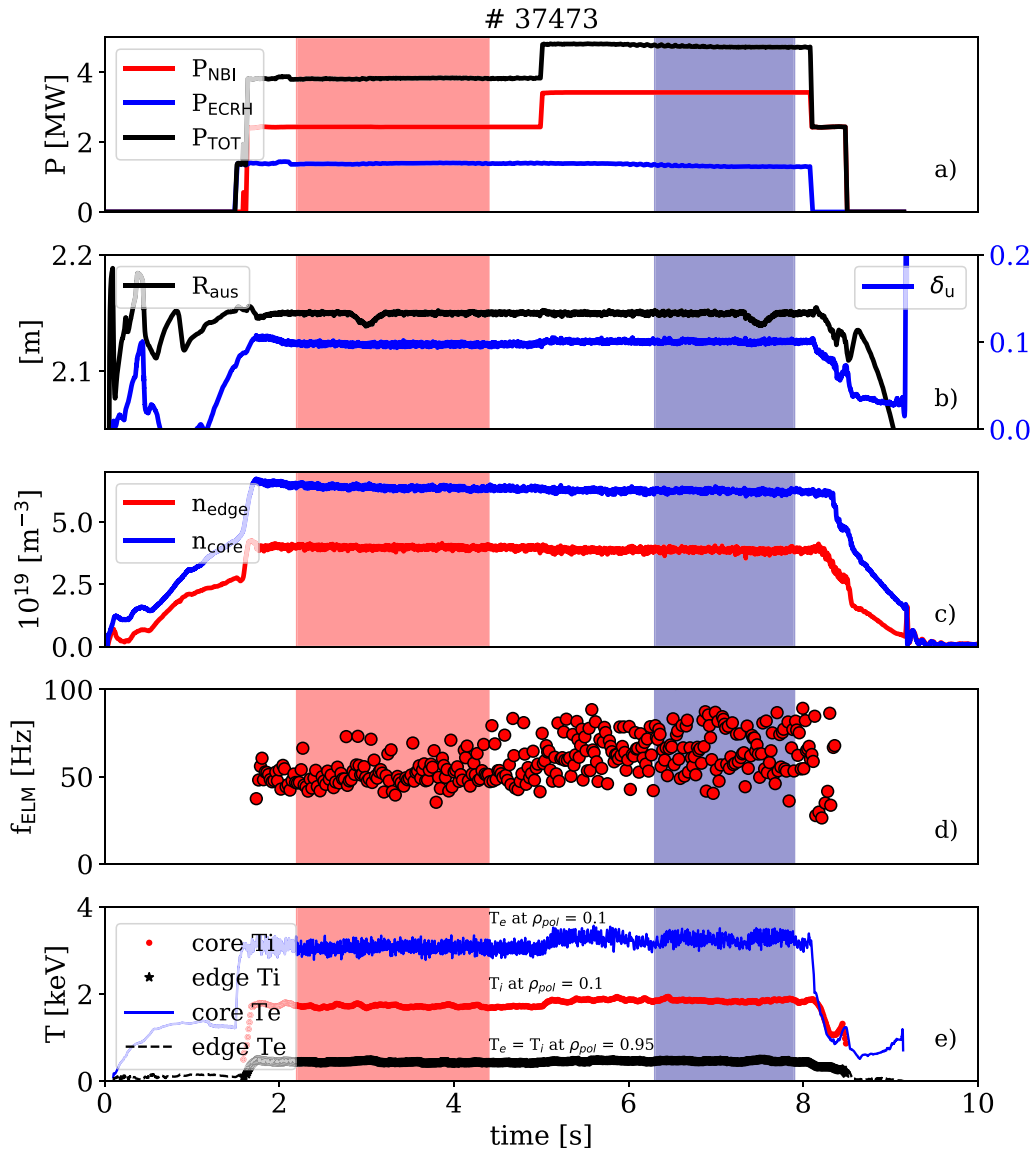


Figure 3. AUG time histories of some of the relevant discharge parameters of the discharge #37473. (a) ECRH (P_{ECRH} in blue), NBI (P_{NBI} in red) and total heating power (P_{TOT} shown in black). (b) Outer plasma boundary (R_{aus}) is shown in black and the upper triangularity (δ_u) displayed in blue. (c) Central (n_{core}) and edge (n_{edge}) densities are displayed in blue and red, respectively. (d) Detected ELM frequency throughout the discharges as evaluated using the divertor shunt current signal. (e) Core Te and Ti evaluated at $\rho_{\text{pol}} = 0.1$ are shown in blue and red, respectively. Edge Ti and Te evaluated at $\rho_{\text{pol}} = 0.95$, shown as black stars and dashes, respectively, are at the same levels.

Table 1. Time interval, ECRH heating power (P_{ECRH}), neutral beam injected power (P_{NBI}), total heating power (P_{TOT}) and the upper triangularity (δ_u) for the discharge #37473 shown in figure 3.

#	Time (s)	P_{ECRH} (MW)	P_{NBI} (MW)	P_{TOT} (MW)	Upper triangularity δ_u
Phase 1	2.2–4.4	1.2	2.5	3.7	0.095
Phase 2	6.3–7.8	1.2	3.5	4.7	0.095

figure 3(d) and shows a slight increase as the additional 1 MW of heating power is introduced. Figure 3(e) shows electron and ion core and edge temperatures, respectively. While the core electron temperature (blue) differs from the core ion temperature (red), the ion and the electron temperatures overlap at the plasma edge (black). In this experiment, the tangential NBI source operated from $t = 1.594$ to 8.492 s at full acceleration voltage with 2.5 MW delivered heating power. At 5 s, an

additional 1 MW of heating power is added from a different NBI source. Both beam boxes operated with deuterium. An additional heating power is delivered to the plasma core via two ECRH sources at 140 GHz and 1.47 MW of ECRH power. Table 1 summarizes the phases and parameters of interest. With the injection of an additional 1 MW of heating power, the toroidal rotation of measured nitrogen impurities increases as shown in figure 4. Red symbols correspond to the rotation

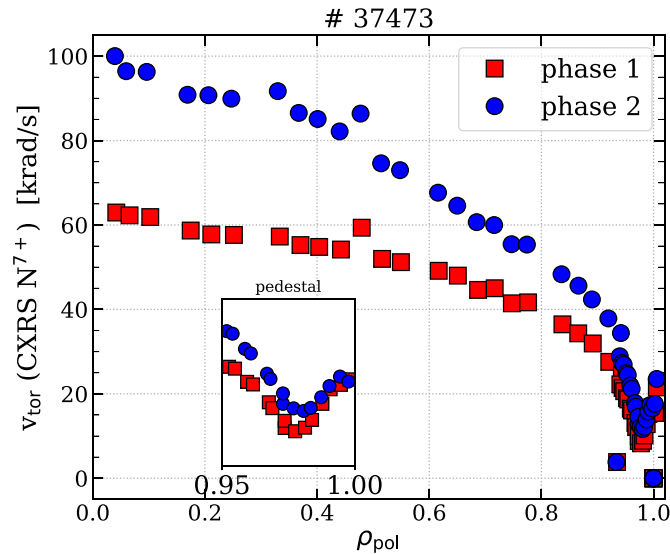


Figure 4. AUG #37473: Profiles of the toroidal rotation of impurities measured with charge exchange recombination spectroscopy. Color-coded data are evaluated during two phases with lower and higher NBI power shown in red and blue, respectively. The profiles at the plasma edge are shown in zoomed view for clarity.

profiles of phase one and blue of phase two. The rotation increases across the entire plasma region, with a more pronounced increase in the core. The edge region has pronounced shear in the rotation that is usually observed in H mode plasma in ASDEX Upgrade [32].

4. Signatures of modes and their location in the pedestal

A typical example of the mode signature is shown in figure 5(a) where the time evolution of one ECEI channel is displayed in blue alongside the divertor shunt current (I_{div}) measurement in black. An initial short and large spike of divertor current I_{div} , typical for an ELM crash, is followed by the second smaller peak. The smaller peak in I_{div} could result from the instantaneous recycling of the ions from the ELM and reaching the main chamber walls [33]. The amplitude of the relative fluctuations in the ECEI signal sharply increases approximately around the time of the appearance of the second smaller peak in I_{div} suggesting potential interplay between the mode behavior at the midplane and the divertor current. The time history of a minimum pressure gradient is shown in figure 5(b) as a solid black line, and it can be seen that the beginning of the phase of minimal pressure gradient coincides with an increase in the mode amplitude and the second peak in the divertor current signal. The timing around those three events is marked with vertical blue lines.

In the experiments reported in [12], the measured toroidal mode numbers of low-frequency modes are $n = 13, 14$, resulting in high poloidal mode numbers for edge modes and, in addition, the associated magnetic perturbations are not measured on the high-field side, suggesting its ballooning nature. In the discharge reported in this manuscript, the modes are not visible in the measurement of the magnetic pick-up coils, and this is likely due to the position of the outer plasma boundary

being further away from the magnetic coils. The magnetic field components in the vacuum approximation falls-off as $B_X \approx (r_{\text{res}}/r_{\text{coil}})^{(m+1)}$ [34] (chapter 3), where r_{res} is the distance to the resonant surface and r_{coil} is the distance to the coil position. Therefore the further away the plasma is from the coils, the mode amplitudes are weakened, especially for high poloidal mode numbers, m . To quantify the change in mode frequency with heating power for this experiment, we show figure 6 where the power spectral density (PSD) of a single channel from the correlation ECE diagnostic is compared between the two phases marked in figure 3. The red color is used for phase 1 and blue for phase 2. The data is averaged over the period displayed in table 2, and ELMs are filtered out. The peak of the PSD curve represents the average mode frequency. The broadening of the PSD around the central frequency corresponds to variations in frequency during the lifetime of modes and for different inter-ELM periods. The average parameters of modes are shown in table 2.

The correlation ECE diagnostic is a powerful tool for mode localization, as it has the highest radial resolution of all present ECE systems at ASDEX Upgrade [22, 35]. The channels are between 4.5 to 5 mm apart in the edge region, and the radial resolution is 4 mm. The strength of temperature fluctuations is approximated by the radial displacement $\xi(r) = \delta T / -T'$, where δT are fluctuation levels and $T' = dT/dr$ is the gradient of the electron temperature. Originally the radial displacements is associated with the temperature perturbations due to tearing modes as defined in [36]. During the phase of lower rotation (phase 1), the fluctuation is distinguished from the noise in multiple channels covering the region of ρ_{pol} between 0.97 and 0.98, and the average radial displacement is about 5.5 mm. With increased rotation (phase 2), the maximum fluctuation amplitude shifts outwards and peaks in the ρ_{pol} region between 0.975 and 0.985. The radial displacement peak is shared equally between two adjacent channels and is about 3–3.5 mm. The strongest displacement

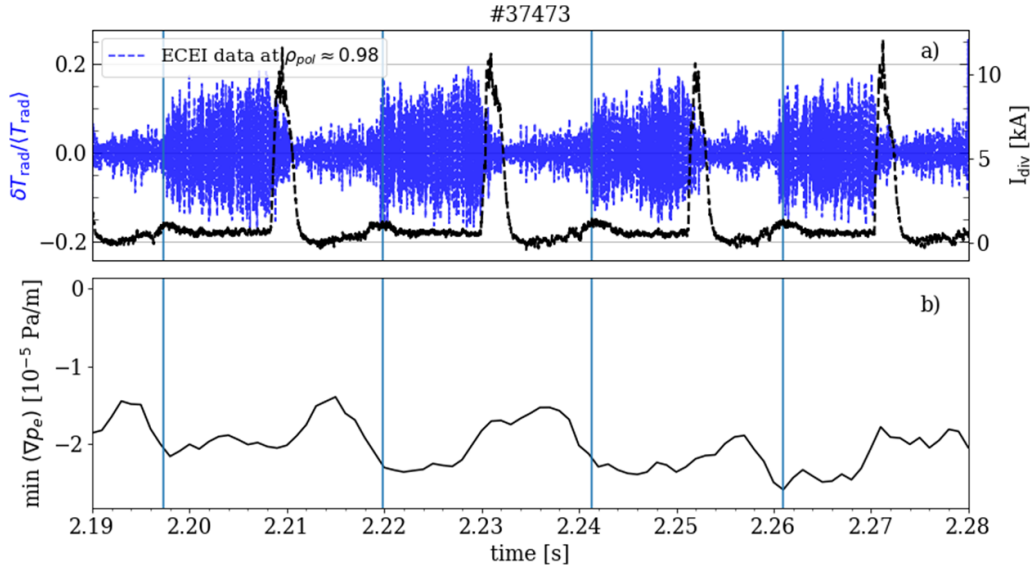


Figure 5. AUG #37473. (a) Time trace of one ECEI channel measuring $\delta T_{\text{rad}}/\langle T_{\text{rad}} \rangle$ at the location of $\rho_{\text{pol}} \approx 0.98$ is shown in blue. A Fourier band-pass filter in the range of 3–18 kHz is applied to this data. The divertor shunt current I_{div} is displayed in black. Large peaks in the divertor current correspond to an ELM crash. (b) Time evolution of the minimum pressure gradient is displayed as a solid black line. Vertical blue lines mark the maximum in the second peak in the divertor shunt current.

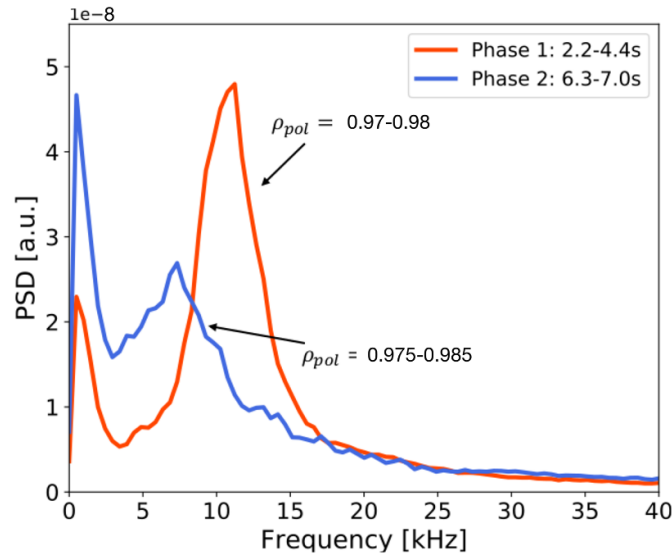


Figure 6. Shot #37473: Power spectrum of a channel #13 of correlation ECE. Phase 1 is shown in red, and phase 2 is in blue. The radial extent in poloidal flux coordinates of the fluctuation is displayed for each phase.

Table 2. Characteristic values of the discharge during the phases of interests: time interval, injected neutral beam power P_{NBI} , upper triangularity δ_u , measured frequency of modes f , and associated radial displacement $\xi(r)$.

Shot #	Time (s)	P_{NBI} (MW)	δ_u	f (kHz)	ξ (mm)
37473	2.2–4.4	2.5	0.095	12.5	5
37473	6.3–7	3.5	0.095	7	3.5

areas are shown in red and blue rectangles alongside the electrons' temperature, density and pressure profiles, displayed in figure 7, respectively. The profiles of n_e , T_e and p_e are obtained by combining different profile diagnostics at ASDEX Upgrade in the framework of IDA [30] as explained

in section 2. The profiles stay constant within the error bars and across the steep gradient region when increasing the heating power, as seen in figure 7. In both phases, the mode is measured to be the strongest in the upper part of the pedestal.

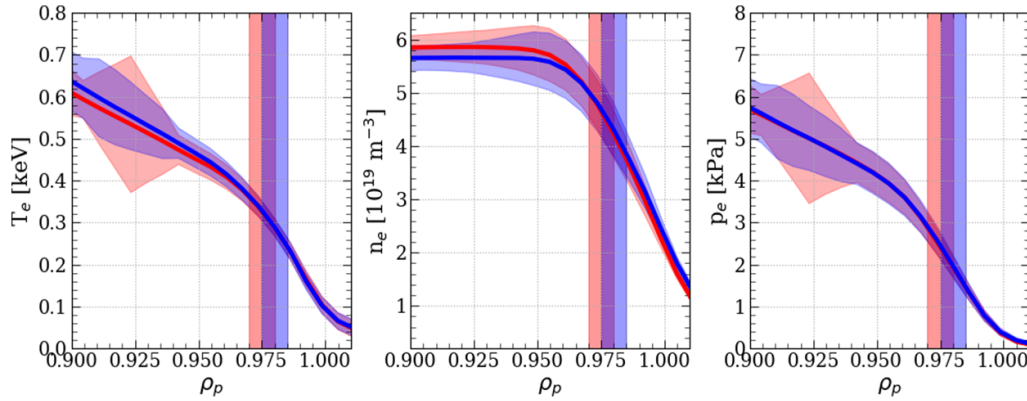


Figure 7. AUG #37473: Profiles of the electron temperature T_e , electron density n_e , and electron pressure p_e averaged over the two time periods indicated in the table 1.

5. Velocity of modes

The mode rotation in the frame of reference of the measuring instrument is determined by the perpendicular fluid velocity $v_{E \times B}$ and the phase velocity v_{ph} . The phase velocity of modes in the pedestal is often associated with half of the ion-diamagnetic flow $v_{i,*}$ [37, 38]. It can, however, be associated with the electron diamagnetic flow $v_{e,*}$ [39]. The phase velocity is a way of identifying the modes as propagation direction is a unique signature of the instabilities [40].

The perpendicular $v_{E \times B}$ velocity is inferred from measurements of the rotation of impurities that can be injected or naturally present in the plasma. Rotation profiles are measured with CXRS [41]. In this experiment, adding nitrogen aids this spectroscopic method. The radial electric field E_r is inferred from the radial force balance equation for N^{7+} impurities and the $E \times B$ drift velocity is calculated as:

$$v_{E \times B} = \frac{E_r}{B} = \frac{1}{B} \left(v_{\phi, N^{7+}} B_{\theta} - v_{\theta, N^{7+}} B_{\phi} + \frac{\nabla p_{N^{7+}}}{e Z_{N^{7+}} n_{N^{7+}}} \right) \quad (1)$$

where v_{ϕ} is toroidal and v_{θ} is the poloidal rotation of measured impurities. B_{ϕ} and B_{θ} are toroidal and poloidal fields, respectively. While the poloidal and toroidal rotation differs among species, the $E \times B$ velocity is common to all species. It can be measured using equation (1) for an arbitrary impurity.

The velocity of modes in the laboratory reference frame is measured with the ECEI system and consists of the velocity of the plasma flow and the phase velocity of the mode $v_{ECEI} = v_{E \times B} + v_{phase}$.

Figure 8 displays time-resolved images of the poloidal cross-section during $50 \mu s$ of the discharge #37473. The data is band-pass Fourier filtered in the range between 5 and 20 kHz to enhance the fluctuations caused by the mode. The mode has characteristic minima and maxima and propagates upwards in the poloidal plane in the electron diamagnetic flow direction. We obtain typical structures of modes with such images and compare them between the two phases as shown in figure 9. The local poloidal wavelength $\lambda_{pol, ECEI}$ changes between those two cases. In phase 1 $\lambda_{pol, ECEI} \sim 20$ cm while in the phase

with higher heating $\lambda_{pol, ECEI} \sim 40$ cm. Using this information and considering that the modes in both phases are localized at a specific q value, we can estimate the poloidal mode number m . The straight field line angle θ^* is used as a poloidal coordinate. With this approach, we remove the distortion of modes due to the shaping effects as suggested in [42] and applied to the case of ECE Imaging in [43]. With this in mind, we calculate the poloidal mode number as $m = 2\pi / \Delta\theta^*$ for both phases. During phase 1, the poloidal mode number is $m = 89 \pm 17$. With the safety factor at the location of the mode $q = 5$, the estimated toroidal mode number during phase one is $n = 17 \pm 3$. In phase two, the poloidal mode number decreases to $m = 43 \pm 9$, and so does the toroidal mode number $n = 9 \pm 2$, with safety factor $q = 5.2$ at the location of the mode.

The apparent poloidal velocities at the outboard mid-plane measured with the ECEI are of the order of $v_{ECEI} \sim 2.4 \pm 0.55$ km s $^{-1}$ in phase 1 and $v_{ECEI} \sim 3 \pm 0.8$ km s $^{-1}$ in phase 2. The velocity and poloidal wavelength uncertainties are determined as the standard deviation from the measurements. Considering that the ECEI measures velocities in a poloidal plane and that the $E \times B$ and the diamagnetic velocities are velocities perpendicular to the field, it follows that $v_{ECEI} = v_{\perp, mode} \cos(\alpha)$. The pitch angle α is defined as the ratio between the poloidal and toroidal field and is obtained using relation $\alpha = \arctan(B_{pol} / B_{tor})$. In addition $v_{\perp, mode} = v_{E \times B} + v_{phase}$, therefore $\frac{v_{ECEI}}{\cos \alpha} = v_{E \times B} + v_{ph}$.

At last, we compare $E \times B$ velocity with measurements of the ECE Imaging projected onto a perpendicular plane as shown in figure 10. Figure- 10 shows ELM filtered radial electric field E_r profiles (left) and calculated $E \times B$ velocity (right), respectively. The filled circles in figure 10(right) correspond to the ECE Imaging measurements. During phase 1 (in red), the mode is localized around $v_{E \times B} = 0$; therefore, the measured mode velocity of about -2.5 km s $^{-1}$ could be entirely attributed to the phase velocity in the electron diamagnetic direction. However, there is a level of ambiguity due to the uncertainty in the localization. Phase 2 (in blue) shows the measured mode velocity equal to the $E \times B$ velocity. The phase velocity could be zero, but the same ambiguity remains. It also should

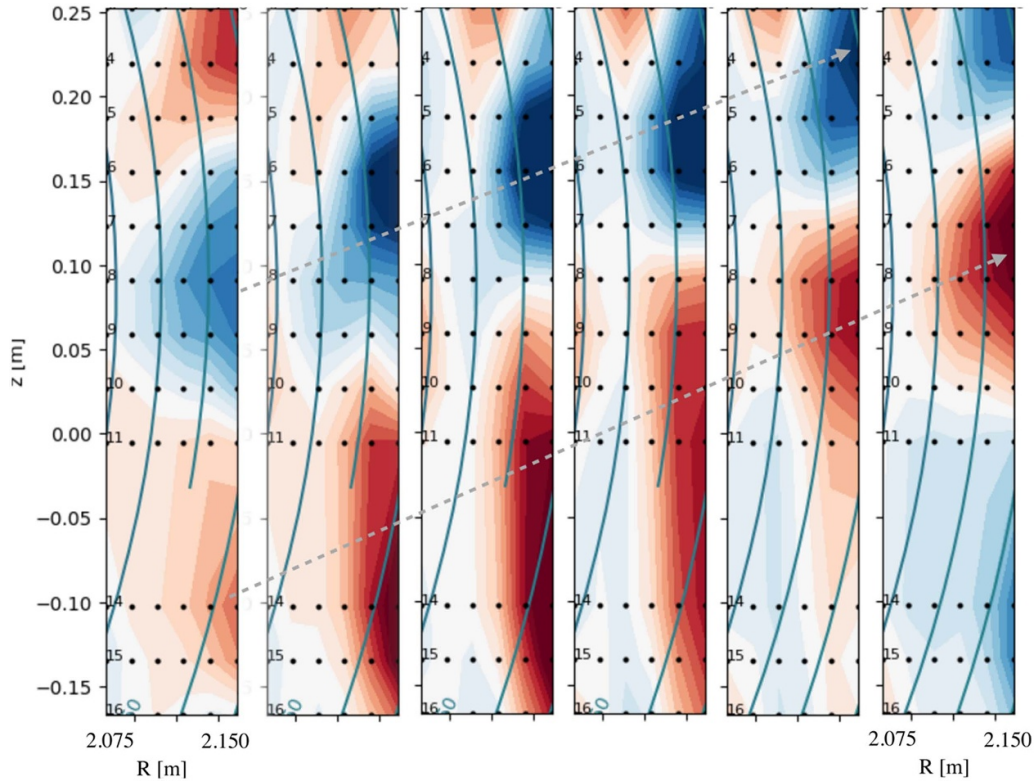


Figure 8. Shot #37473: Time-resolved snapshots of the edge region measured with the electron cyclotron emission imaging instrument. Relative temperature fluctuations propagate in a waveform with visible maxima and minima. Note that the region between -0.1 m and 0 m in a poloidal plane is interpolated due to malfunctioning detectors.

be noted that the instantaneous mode velocity and structure can change during a single inter-ELM.

6. Modelling

To assess the effect that the NBI heating power and hence the toroidal rotation can have on inter-ELM modes, the two scenarios described above are modeled using the CASTOR3D code [44, 45]. The CASTOR3D code is a resistive linear MHD stability code and includes plasma rotation, parallel viscosity, and gyro-viscosity. The CASTOR3D code is based on a single-fluid set of equations where the ion velocity is given as:

$$\vec{V}_i = \underbrace{\frac{\vec{E} \times \vec{B}}{B^2}}_{=\vec{V}_E} + \underbrace{\vec{v} \cdot \frac{\vec{B}}{B}}_{=\vec{V}_\parallel} + \alpha \underbrace{\frac{1}{\rho} \frac{\vec{B} \times \nabla p_i}{B^2}}_{=\vec{V}_i^*} \quad (2)$$

where $\vec{V}_{\text{MHD}} = \vec{V}_E + \vec{V}_\parallel$ is the MHD velocity, \vec{V}_i^* is the ion diamagnetic drift velocity. The equation (2) can be decomposed in poloidal and toroidal components for each velocity contribution and written as a sum of those as $\vec{V}_i = \vec{V}_{\text{pol}} + \vec{V}_{\text{tor}}$. In the current version of CASTOR3D code, the poloidal components are considered zero, and the remaining part is the velocity in the toroidal direction.

The pressure gradient profile and corresponding resistivity profiles used in the modeling are shown in figure 11. Red profiles are related to phase 1 with lower NBI heating and rotation, while the blue profiles belong to phase 2 with higher NBI heating and rotation. The pressure profiles and corresponding gradient are based on equilibrium reconstruction with CLISTE [46], while the neoclassical resistivity is calculated using formula as defined in [47]. A final result of the modeling is shown in figure 12. Figure 12(a) shows the growth rates of modes, and their respective oscillation frequencies are displayed in figure 12(b). Color-coded are the two-time points. Phase 1, the phase with lower toroidal rotation, is represented with red and corresponds to $t = 2.55$ s, while the increased toroidal rotation window is displayed as blue and describes the plasma conditions at $t = 5.92$ s. As demonstrated in figure 12(a) from the red to blue case, the growth rates decrease with an increase in NBI heating power. The mode oscillation frequency is in the kHz range and varies depending on the toroidal mode number. When comparing the two phases, the frequency of modes increases as the injected NBI power increases.

The uncertainties of the growth rates and frequencies were obtained by varying the dynamic viscosity and resistivity within the range of their respective model uncertainties. The most unstable modes are the ones with the toroidal mode numbers in the range $n = 15$ – 24 and are in a similar range for both phases. The most unstable mode in phase 1 is $n = 21$ with oscillation frequency $f = 7$ kHz while the most unstable mode

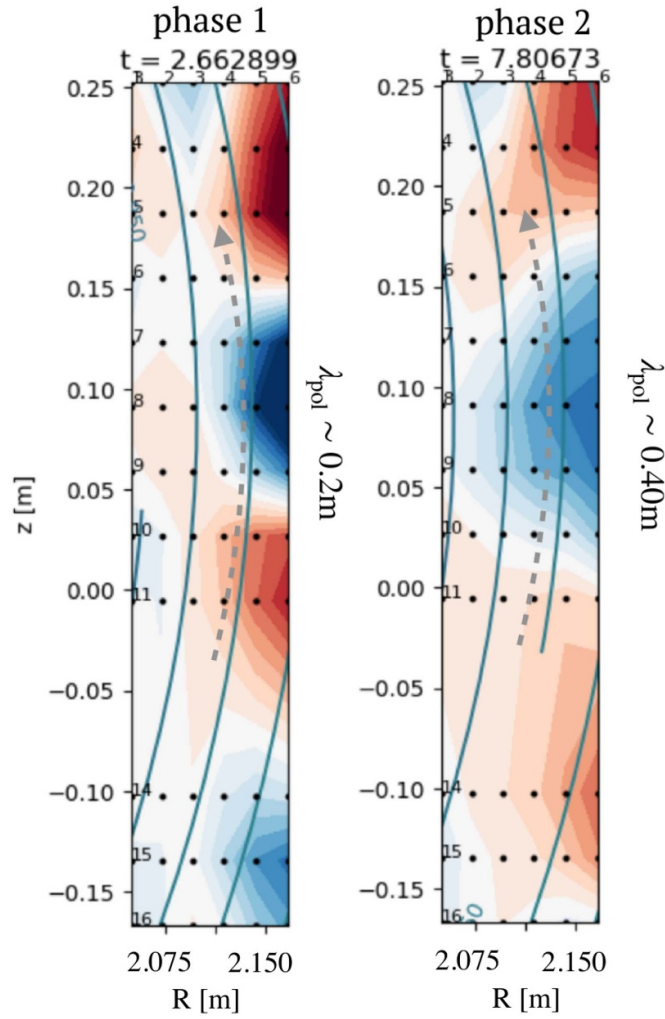


Figure 9. Shot #37473: An example of poloidal mode structure at a single time point measured by the ECEI system. The left figure shows the data during phase 1, and the figure to the right shows the mode structure during phase 2. Note that the region between -0.1 m and 0 m in the poloidal plane is interpolated due to malfunctioning lines of sight.

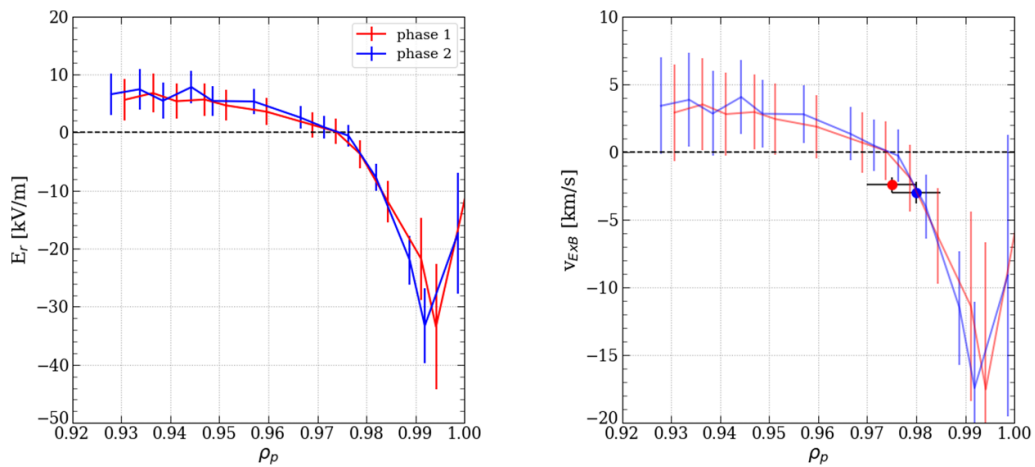


Figure 10. Shot #37473: (left) ELM filtered E_r profiles across the pedestal as inferred by the CXRS measurements. The profiles are averaged during period $t = 2.2$ – 4.4 s shown in red and $t = 6.3$ – 7.5 s in blue. (right) Calculated $E \times B$ velocity. The red and blue circles correspond to the mean value of ten ECEI measurements for phase 1 and 2, respectively.

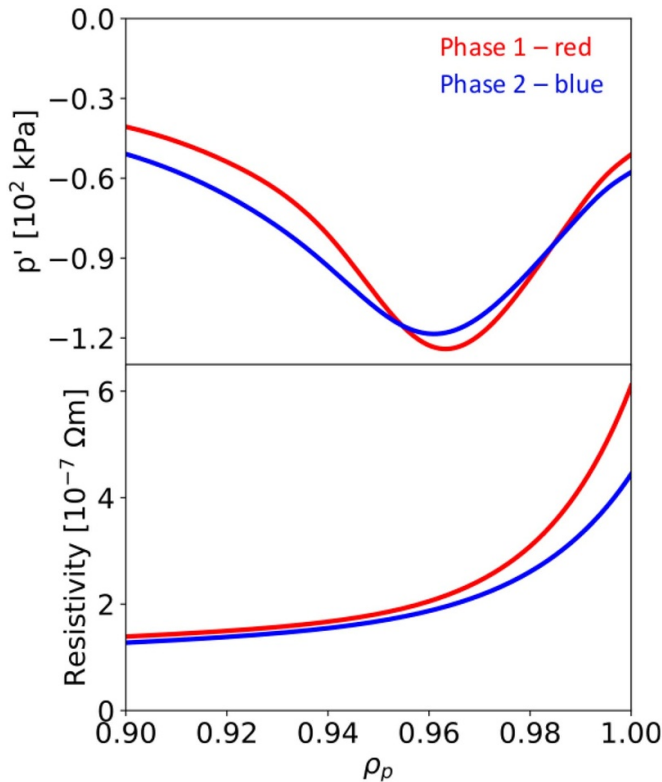


Figure 11. Shot #37473: Pressure gradient profile (top) and resistivity profile (bottom) used for modeling. Color-coded is the single time point in the simulation where red corresponds to the $t = 2.55$ s (phase I), and blue is at $t = 5.92$ s (phase II).

during phase 2 is the mode with toroidal mode number $n = 19$ and oscillation frequency $f = 13$ kHz.

The instabilities obtained in the modeling are located at the low fieldside and are found to be unstable only when considering finite resistivity. This allows for identifying the instabilities as resistive ballooning modes (RBMs). Since the modes become stable for vanishing resistivity, they cannot be described with ideal MHD. The pressure and resistivity profiles used in the modeling shown in figure 11 slightly differ between the two phases. Therefore, to study the effects of such profiles on mode growth rates and their frequency, separate runs with CASTRO3D have been performed. These runs subsequently exchange the velocity and resistivity profiles between the two phases, subscribing the higher rotation profile to phase 1 and the lower rotation profile to phase 2. The same has been done with resistivity. Furthermore, velocity and resistivity have also been exchanged simultaneously, and, in addition, the effect of exchanging the viscosity profiles has been checked. The resulting growth rates and mode frequencies using the abovementioned method are shown in figure 13. The red and the solid blue lines are the original results of the simulation, shown in figure 12, corresponding to the profiles shown in figure 11. The dashed lines are the results of the different profiles being exchanged between the two phases. The top panel of a figure pair shows growth rates, while the bottom plot shows a mode frequency.

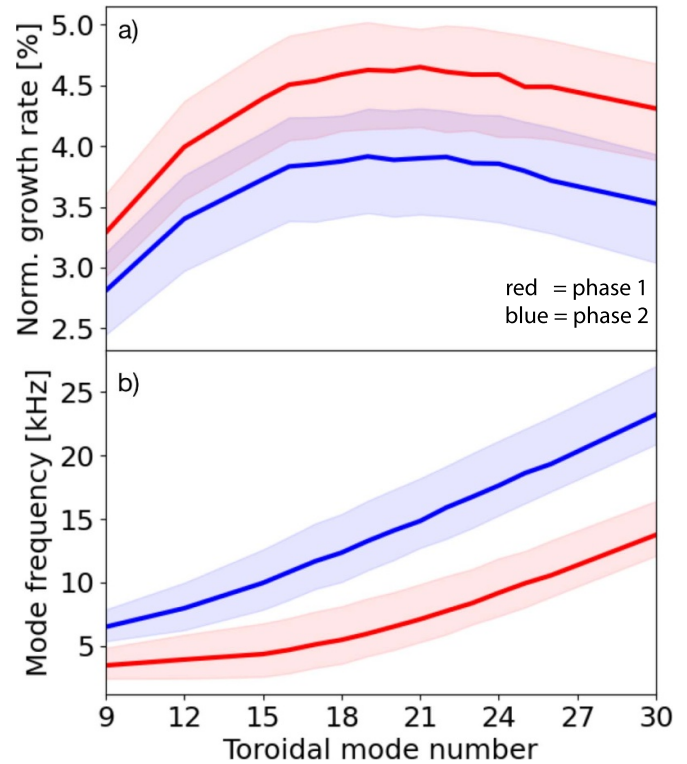


Figure 12. Shot #37473: Growth rates (a) and mode frequencies (b) from CASTOR3D. Color-coded is the single time point from the simulation where red corresponds to the $t = 2.55$ s (phase I), and blue is at $t = 5.92$ s (phase II).

- Exchange of the velocity profiles. Figure 13(a).
The effect on growth rates: The resulting red dashed line is slightly below the original red solid line, which means that the higher rotation profile results in slightly lower growth rates. The blue dashed line is slightly above the original solid blue line, suggesting that an increase in growth rates is due to lowering the rotation profiles and consequently lowering of the shear—the effect of toroidal rotation and its shear on modes with CASTOR3D shows a slight stabilizing effect. A higher rotation and shear profile results in lower growth rates within the error bars.
The effect on mode frequency: The resulting red dashed line corresponding to the higher rotation profile shows an increase compared to the solid red line. In contrast, the resulting dashed blue line is well below the original solid blue line showing that the impact of toroidal rotation on mode frequency results in rotation being completely flipped and outside of the error bars. Therefore, toroidal rotation and mode frequency have a significant positive correlation.
- Exchange of the resistivity profiles. Figure 13(b).
The effect on growth rates: When a lower resistivity profile is used, the growth rates decrease, as shown in the red dashed line. With an increased resistivity profile, the growth rates also increase (blue dashed line). Therefore, a positive correlation exists between the resistivity and growth rates of modes due to their resistive nature. The effect on mode frequency: Resistivity, however, has only marginal influence on the frequency of modes as seen in the bottom plot of

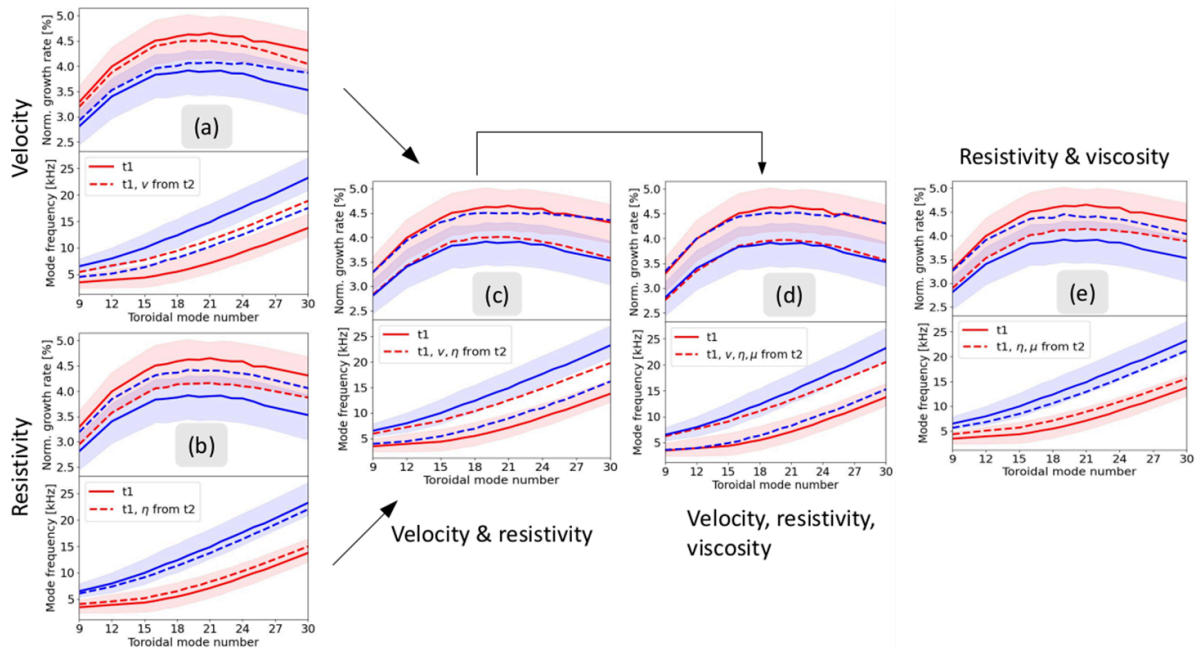


Figure 13. Shot #37473: Figure pair of growth rates (top) and mode frequencies (bottom) for a different set of input profiles resulting from a CASTOR3D simulation. (a) Exchanged velocity profiles between the two phases. (b) Exchanged the resistivity profiles between the two phases. (c) Velocity and resistivity profiles have been exchanged simultaneously in addition to the velocity and resistivity. (e) Resistivity and viscosity profiles are exchanged between the two phases. Solid red and blue lines are shown on each sub-figure and correspond to the original result shown in figure 12 obtained using profiles shown in figure 11 as input. The dashed lines are CASTOR3D results using exchanged profiles.

figure 13(b). The red dashed line is slightly above the solid red line corresponding to the original case, while the blue dashed line is slightly below the original solid blue line.

- Exchange of the velocity and resistivity profiles simultaneously. Figure 13(c).

While in figures 13(a) and (b), we have looked into separate effects of toroidal rotation and resistivity. Their combined effect is shown here.

The effect on growth rates: Using the higher rotation and lower resistivity profile from case #2 results in the growth rate in the dashed red line matching its original form shown in the solid blue line. The same is valid when comparing the original solid red line and a dashed blue line corresponding to exchanged profiles. We conclude that combined rotation and resistivity fully recover their original growth rate behavior, i.e. the difference in growth rates between phase 1 and 2 is fully described by the difference in rotation (shear) and resistivity.

The effect on mode frequency: Frequency obtained using higher rotation and lower resistivity profiles (red dashed line) results in slightly lower mode frequency than the original (solid blue line) result. The mode frequency obtained with lower rotation and higher resistivity (blue dashed line) is slightly higher than its original result (in solid red line).

- Exchange of velocity, resistivity, and viscosity profiles. Figure 13(d)

If we now, in addition to exchanged velocity and resistivity, add exchanged viscosity profile the modeling result is as follows: as shown in the top panel of figure 13(d), the growth rates do not change at all compared to the case where only

the resistivity and velocity were changed. The solid red line coincides with the dashed blue line, and the solid blue line agrees with the red dashed line. A similar trend is valid when looking into mode frequency as shown in the bottom panel of figure 13(d). Therefore, the viscosity profiles do not impact mode growth rates. Compared to figure 13(a), the mode frequency is closely related to its original behavior.

- Exchange of the resistivity and viscosity profiles. Figure 13(e).

The effect on growth rates: Resistivity and viscosity profiles exchange, as shown in figure 13(e), give similar results as in figure 13(b) and confirm that the influence of resistivity on growth rates was correct. The influence of viscosity on growth rates is negligible.

The effect on mode frequency: Again, a similar trend as in 13(b) is obtained; the mode frequency is only slightly influenced by the resistivity and viscosity profile. Thus, while resistivity and viscosity support the difference in mode frequency between phase 1 and 2, the difference is mostly dominantly caused by the rotation profile (figure 13(a)).

7. Discussion and outlook

In this work, we compare the behavior of modes appearing between type-I ELMs with increasing NBI beam power concomitant increase in toroidal rotation to the modeling. Although the experimental conditions are designed to be constant during the discharge, an increase in NBI beam power

can influence density and temperature profiles. Separating such small effects is challenging as those changes are within the experimental error bars. However, the numerical exercise enables us to manipulate input profiles used in the modeling and evaluate the effects on growth rates and mode frequency separately.

The experimentally controlled parameter is toroidal rotation, and with an injection of an additional 1 MW of NBI beam power, the toroidal rotation increases across the plasma radius. An injection of one NBI beam, increasing toroidal rotation, results in lower mode frequency and lower strength of the mode. This has been demonstrated by showing the mode frequency lowering from 12 kHz to 7 kHz, and the radial displacement caused by such modes decreases from 5 mm to 3.5 mm as the toroidal rotation profile increases.

In addition, changes in location and poloidal structure of modes are measured. With increased heating, modes shift radially outwards, and their poloidal mode numbers decrease. The mode velocity is measured to be close to the $E \times B$ velocity. However, due to the uncertainties, final statements about their phase velocity cannot be made.

Linear MHD modeling with CASTOR3D code shows that modes appearing between ELMs are RBMs, as they do not appear unstable without the inclusion of the resistivity. The most unstable toroidal mode numbers are in the range $n = 15\text{--}24$ and are slightly higher than the one found in the experiment. This difference could be due to the absence of poloidal rotation in the model and difference in resistivity profiles between model and the experiment. Modeling results show that the mode growth rates are lower with higher rotation profiles when using experimental velocity profiles prescribed to two different phases. In addition, CASTOR3D output shows that mode frequency increases with increased toroidal rotation.

The experimental measurements acquired during the non-linear saturated phase of modes show that the mode becomes weaker with rotation, and the linear phase of modes is assessed with the CASTOR3D code showing that the growth rates of the most unstable modes decrease with a higher rotation profile. Therefore, the modeling result suggests the stabilizing effect of rotation on an RBM. However, this effect cannot be subscribed to the toroidal rotation. Separate CASTOR3D runs have been performed to access the isolated effects of velocity, resistivity, and viscosity alone on growth rates and mode frequency, as shown in figure 13. Figure 13(b) demonstrates the primary role of resistivity on growth rates and the effect of rotation and its shear is rather small. While the trend between toroidal rotation and displacement in the experiment matches the CASTOR3D trend between toroidal rotation and growth rates, the frequency behavior compared between the experiment and modeling goes in the opposite direction. In the experiment, the mode frequency decreases with rotation, while we observe the opposite in the modeling. This difference is likely caused by the poloidal velocities currently not included in CASTOR3D. Since the poloidal velocities are the dominant contribution to the background velocities in the plasma edge, their contribution is expected to impact the stability of turbulence in H-modes [48]. Nevertheless, a clear indication of rotation velocity playing a role in setting the mode frequency has

been demonstrated in figure 13(a). Viscosity does not significantly impact growth rates and mode frequency, as can be seen in figure 13(d). Since the inclusion of velocity, resistivity, and viscosity profiles recovers the original CASTOR3D result, the influence of small changes in the pressure profiles has yet to be considered. Further effects like the Hall term in Ohm's law could play an additional role. The poloidal velocity (as well as the Hall term) will be taken into account in an upcoming version of the linear MHD code CASTOR3D (J. Puchmayr in preparation, E. Strumberger in preparation). In addition, the comparison is also limited by the range of uncertainties from measurements and models.

The RBMs are thought to be contributing to the increased edge turbulence and transport in L-mode plasma [49, 50] and are also identified in ELM-free plasma with low triangularity [51]. The model based on the resistive interchange instability predicts the critical temperature for the transition from type-III to type-I ELMs in JET as well as the experimentally observed toroidal field dependence of the critical temperature of type III ELMs but model based on resistive ballooning instability reproduces the critical density for observed q_{95} dependence of the transition from type-I to type III-ELMs [52]. Both types of ELMs appear just above the L-H power threshold and exhibit strong MHD precursors, but their frequency responds differently to the input power as discussed in [53].

The work presented in this manuscript shows that the RBMs exist in the edge region of H-mode plasma with type-I ELMs. They become unstable while the pressure gradient is clamped, long before the pressure gradient reaches the ideal peeling-ballooning threshold. Theoretical estimates of the transport effects caused by the RBMs have been discussed in [49, 54] and are found to be mainly thermal electron conduction losses. However, any estimates of transport caused by RBMs between type-I ELMs at ASDEX Upgrade tokamak and their role in regulating the pressure gradient can only be subject to the non-linear models and are left for further investigation.










Data availability statement

The data that support the findings of this study are available upon reasonable request from the authors.

Acknowledgments

This work is supported by the US DOE under Award DE-SC0014264. This work has been carried out within the framework of the EUROfusion Consortium, funded by the European Union via the Euratom Research and Training Programme (Grant Agreement No. 101052200—EUROfusion). Views and opinions expressed are however those of the author(s) only and do not necessarily reflect those of the European Union or the European Commission. Neither the European Union nor the European Commission can be held responsible for them.

ORCID iDs

B Vanovac  <https://orcid.org/0000-0003-4031-9318>
 J Puchmayr  <https://orcid.org/0000-0001-5257-7483>
 R Bielajew  <https://orcid.org/0000-0002-9578-368X>
 M Willensdorfer  <https://orcid.org/0000-0002-1080-4200>
 E Wolfrum  <https://orcid.org/0000-0002-6645-6882>
 M Cavedon  <https://orcid.org/0000-0002-0013-9753>
 E Strumberger  <https://orcid.org/0009-0004-0796-2381>
 M G Dunne  <https://orcid.org/0000-0002-5259-9970>
 W Suttrop  <https://orcid.org/0000-0003-0983-8881>

References

- [1] Hassam A B, Antonsen T M, Drake J F and Guzdar P N 1990 Theory of ion temperature gradient instabilities: thresholds and transport *Phys. Fluids B* **2** 1822–32
- [2] Dong J Q, Sanuki H, Itoh K and Chen L 2002 Electron temperature gradient instability in toroidal plasmas *Phys. Plasmas* **9** 4699–708
- [3] Xiao Y and Lin Z 2009 Turbulent transport of trapped-electron modes in collisionless plasmas *Phys. Rev. Lett.* **103** 085004
- [4] Hatch D R, Kotschenreuther M, Mahajan S, Valanju P, Jenko F, Told D, Görler T and Saarelma S 2016 Microtearing turbulence limiting the JET-ILW pedestal *Nucl. Fusion* **56** 104003
- [5] Loarte A *et al* 2003 Characteristics of type I ELM energy and particle losses in existing devices and their extrapolation to ITER *Plasma Phys. Control. Fusion* **45** 1549
- [6] Kong D F *et al* (HL-2A Team) 2018 Dynamics of the pedestal in the recovery phase between type-III ELMS *Nucl. Fusion* **58** 034003
- [7] Koslowski H R, Alper B, Borba D N, Eich T, Sharapov S E, Perez C P and Westerhof E JET-EFDA contributors 2005 Observation of the palm tree mode, a new MHD mode excited by type-I ELMS on JET *Nucl. Fusion* **45** 201
- [8] Perez C P *et al* (JET EFDA contributors) 2003 Washboard modes as ELM-related events in JET *Plasma Phys. Control. Fusion* **46** 61
- [9] Suttrop W, Büchl K, de Blank H J, Schweinzer J and Zohm H (ASDEX Upgrade team, NBI group and ICRH group) 1996 Characteristics of edge localized modes in ASDEX Upgrade *Plasma Phys. Control. Fusion* **38** 1407–10
- [10] Colton A L, Buttery R J, Fielding S J, Gates D A, Hender T C, Huggill J, Morris A W and Valovic M (The COMPASS-D and ECRH teams) 1996 ELM studies on the COMPASS-D tokamak *Plasma Phys. Control. Fusion* **38** 1359
- [11] Bolzonella T, Zohm H, Maraschek M, Martinez E, Saarelma S and Günter S ASDEX Upgrade Team 2004 High frequency MHD activity related to type I ELMS in ASDEX Upgrade *Plasma Phys. Control. Fusion* **46** A143
- [12] Vanovac B *et al* (The ASDEX Upgrade Team) 2018 Characterization of low-frequency inter-ELM modes of H-mode discharges at ASDEX Upgrade *Nucl. Fusion* **58** 112011
- [13] Laggner F M *et al* (The EUROfusion MST1 Team and the ASDEX Upgrade Team) 2016 High frequency magnetic fluctuations correlated with the inter-ELM pedestal evolution in ASDEX Upgrade *Plasma Phys. Control. Fusion* **58** 065005
- [14] Mink F, Wolfrum E, Maraschek M, Zohm H, Horváth L'ó, Laggner F M, Manz P, Viezzer E and Stroth U the ASDEX Upgrade Team 2016 Toroidal mode number determination of ELM associated phenomena on ASDEX Upgrade *Plasma Phys. Control. Fusion* **58** 125013
- [15] Cai H, Cao J and Li D 2017 Influence of toroidal rotation on tearing modes *Nucl. Fusion* **57** 056006
- [16] Chu M S, Chen L, Zheng L-J, Ren C and Bondeson A 1999 Effect of rotation on ideal and resistive MHD modes *Nucl. Fusion* **39** 2107–11
- [17] Cheng S, Zhu P and Banerjee D 2017 Enhanced toroidal flow stabilization of edge localized modes with increased plasma density *Phys. Plasmas* **24** 092510
- [18] Bondeson A and Ward D J 1994 Stabilization of external modes in tokamaks by resistive walls and plasma rotation *Phys. Rev. Lett.* **72** 2709–12
- [19] Wahlberg C and Bondeson A 2001 Stabilization of the Mercier modes in a tokamak by toroidal plasma rotation *Phys. Plasmas* **8** 3595–604
- [20] Burrell K H, Osborne T H, Snyder P B, West W P, Fenstermacher M E, Groebner R J, Gohil P, Leonard A W and Solomon W M 2009 Edge pedestal control in quiescent H-mode discharges in DIII-D using co-plus counter-neutral beam injection *Nucl. Fusion* **49** 085024
- [21] Snyder P B *et al* 2007 Stability and dynamics of the edge pedestal in the low collisionality regime: physics mechanisms for steady-state ELM-free operation *Nucl. Fusion* **47** 961–8
- [22] Creely A J, Freethy S J, Burke W M, Conway G D, Leccacorvi R, Parkin W C, Terry D R and White A E 2018 Correlation electron cyclotron emission diagnostic and improved calculation of turbulent temperature fluctuation levels on ASDEX Upgrade *Rev. Sci. Instrum.* **89** 053503
- [23] Vanovac B, Denk S S, Wolfrum E, Willensdorfer M, Suttrop W, Fischer R and Luhmann N C (ASDEX Upgrade Team) 2019 Mode analysis limitations of ECE-I and ECE measurements at the plasma edge *EPJ Web Conf.* **203** 02011
- [24] Denk S S *et al* (The ASDEX Upgrade Team) 2018 Analysis of electron cyclotron emission with extended electron cyclotron forward modeling *Plasma Phys. Control. Fusion* **60** 105010
- [25] Classen I G J *et al* 2010 2D electron cyclotron emission imaging at ASDEX Upgrade (invited) *Rev. Sci. Instrum.* **81** 10D929
- [26] Classen I G J, Domier C W, Luhmann N C, Bogomolov A V, Suttrop W, Boom J E, Tobias B J and Donné A J H 2014 Dual array 3D electron cyclotron emission imaging at ASDEX Upgrade *Rev. Sci. Instrum.* **85** 11D833
- [27] Fonck R J, Darrow D S and Jaehnig K P 1984 Determination of plasma-ion velocity distribution via charge-exchange recombination spectroscopy *Phys. Rev. A* **29** 3288–309
- [28] Viezzer E, Pütterich T, Dux R and McDermott R M 2012 High-resolution charge exchange measurements at ASDEX Upgrade *Rev. Sci. Instrum.* **83** 103501
- [29] Fischer R and Dinklage A 2007 The concept of integrated data analysis of complementary experiments *AIP Conf. Proc.* **954** 195–202
- [30] Fischer R, Fuchs C J, Kurzan B, Suttrop W and Wolfrum E (ASDEX Upgrade Team) 2010 Integrated data analysis of profile diagnostics at ASDEX Upgrade *Fusion Sci. Technol.* **58** 675–84
- [31] Vanovac B 2019 Low-frequency inter-ELM pedestal modes at ASDEX Upgrade *PhD Thesis* Technische Universiteit Eindhoven Proefschrift
- [32] Pütterich T, Wolfrum E, Dux R and Maggi C F 2009 Evidence for strong inversed shear of toroidal rotation at the edge-transport barrier in the ASDEX Upgrade *Phys. Rev. Lett.* **102** 025001
- [33] Wischmeier M, Kallenbach A, Chankin A V, Coster D P, Eich T, Herrmann A and Müller H W 2007 High recycling outer divertor regimes after type-I ELMS at high density in ASDEX Upgrade *J. Nucl. Mater.* **363–365** 448–52

- [34] Igochine V 2014 *Active Control of Magneto-hydrodynamic Instabilities in Hot Plasmas Springer Series on Atomic, Optical and Plasma Physics* (Springer)
- [35] Freethy S J, Conway G D, Classen I, Creely A J, Happel T, Köhn A, Vanovac B and White A E 2016 Measurement of turbulent electron temperature fluctuations on the ASDEX Upgrade tokamak using correlated electron cyclotron emission *Rev. Sci. Instrum.* **87** 11E102
- [36] Fitzpatrick R 1995 Helical temperature perturbations associated with tearing modes in tokamak plasmas *Phys. Plasmas* **2** 825–38
- [37] Morales J A *et al* 2016 Edge localized mode rotation and the nonlinear dynamics of filaments *Phys. Plasmas* **23** 042513
- [38] Bécoulet M *et al* 2017 Non-linear MHD modelling of edge localized modes dynamics in KSTAR *Nucl. Fusion* **57** 116059
- [39] Wang H Q *et al* 2014 New edge coherent mode providing continuous transport in long-pulse H-mode plasmas *Phys. Rev. Lett.* **112** 185004
- [40] Manz P, Boom J E, Wolfrum E, Birkenmeier G, Classen I G J, Luhmann N C and Stroth U (The ASDEX Upgrade Team) 2014 Velocimetry analysis of type-I edge localized mode precursors in ASDEX Upgrade *Plasma Phys. Control. Fusion* **56** 035010
- [41] Cavedon M, Putterich T, Viezzer E, Dux R, Geiger B, McDermott R M, Meyer H and Stroth U 2017 A fast edge charge exchange recombination spectroscopy system at the ASDEX Upgrade tokamak *Rev. Sci. Instrum.* **88** 043103
- [42] Schittenhelm M and Zohm H 1997 Analysis of coupled MHD modes with Mirnov probes in ASDEX Upgrade *Nucl. Fusion* **37** 1255
- [43] Boom J E *et al* (The ASDEX Upgrade Team) 2011 2D ECE measurements of type-I edge localized modes at ASDEX Upgrade *Nucl. Fusion* **51** 103039
- [44] Strumberger E and Günter S 2016 CASTOR3D: linear stability studies for 2D and 3D tokamak equilibria *Nucl. Fusion* **57** 016032
- [45] Strumberger E and Günter S 2019 Linear stability studies for a quasi-axisymmetric stellarator configuration including effects of parallel viscosity, plasma flow and resistive walls *Nucl. Fusion* **59** 106008
- [46] Mc Carthy P J (ASDEX Upgrade Team) 2011 Identification of edge-localized moments of the current density profile in a tokamak equilibrium from external magnetic measurements *Plasma Phys. Control. Fusion* **54** 015010
- [47] Redl A, Angioni C, Belli E and Sauter O (ASDEX Upgrade Team and EUROfusion MST1 Team) 2021 A new set of analytical formulae for the computation of the bootstrap current and the neoclassical conductivity in tokamaks *Phys. Plasmas* **28** 022502
- [48] Sasaki M, Itoh K, Kosuga Y, Dong J Q, Inagaki S, Kobayashi T, Cheng J, Zhao K J and Itoh S-I 2019 Parallel flow driven instability due to toroidal return flow in high-confinement mode plasmas *Nucl. Fusion* **59** 066039
- [49] Rafiq T, Bateman G, Kritz A H and Pankin A Y 2010 Development of drift-resistive-inertial ballooning transport model for tokamak edge plasmas *Phys. Plasmas* **17** 082511
- [50] Cohen B I, Umansky M V, Nevins W M, Makowski M A, Boedo J A, Rudakov D L, McKee G R, Yan Z and Groebner R J 2013 Simulations of drift resistive ballooning L-mode turbulence in the edge plasma of the DIII-D tokamak *Phys. Plasmas* **20** 055906
- [51] Cathey A, Hoelzl M, Harrer G, Dunne M G, Huijsmans G T A, Lackner K, Pamela S J P, Wolfrum E and Günter S (The JOREK Team, the ASDEX Upgrade Team and the EUROfusion MST1 Team) 2022 MHD simulations of small ELMS at low triangularity in ASDEX Upgrade *Plasma Phys. Control. Fusion* **64** 054011
- [52] Sartori R *et al* 2004 Study of type III ELMS in JET *Plasma Phys. Control. Fusion* **46** 723
- [53] Zohm H 1996 Edge localized modes (ELMs) *Plasma Phys. Control. Fusion* **38** 105–28
- [54] Carreras B A *et al* 1983 Transport effects induced by resistive ballooning modes and comparison with high- β_p ISX-B tokamak confinement *Phys. Rev. Lett.* **50** 503–6